Published in final edited form as:
IEEE Trans Nucl Sci. 2000 June 1; 47(3): 1112–1117.

Static Versus Dynamic Teboroxime Myocardial Perfusion SPECT in Canines[1]

D.J. Kadrmas, **E.V.R. Di Bella**, **H.S. Khare**, **P.E. Christian**, and **G.T. Gullberg**
Medical Imaging Research Laboratory, Department of Radiology, 729 Arapeen Dr., Salt Lake City, UT 84108-1218

Abstract

Tc-99*m*-teboroxime is a perfusion tracer with high myocardial extraction, fast washin and washout kinetics, and excellent imaging properties. The fast kinetics pose some problems for static imaging, but they also allow for back-to-back stress / rest studies to be performed very quickly. Furthermore, such fast kinetics are ideally suited for dynamic imaging. We have compared static versus dynamic myocardial perfusion SPECT with teboroxime in canines using microsphere-derived flow values as the gold standard. Dynamic data were successfully acquired at rest and under adenosine stress in seven dogs using a fast serial scanning protocol. The data were analyzed in two ways: summing timeframes to create a single, static dataset with consistent projections; and 4D reconstruction and kinetic parameter estimation for a two compartment model. In both cases imaging data (voxel intensity or washin rate parameter) were correlated with flow values measured by microspheres. The static summing procedure that produced the best correlation with flow consisted of summing the projection data acquired from 60 to 180 seconds post–injection. The washin rate parameter was found to provide better correlation with flow than static image intensity in six of seven animals. When the data were pooled over all studies, washin provided significantly better correlation with flow than static imaging ($p<0.01$). We conclude that dynamic imaging of teboroxime with compartmental modeling provides a better measure of flow than can be obtained from static imaging techniques.

I. INTRODUCTION

Technetium-99*m* labeled teboroxime is a neutral lipophilic compound with high myocardial extraction and rapid washout kinetics that has been investigated as a tracer for myocardial perfusion SPECT [1]. Teboroxime has a number of desirable properties that may make it more efficacious than thallium-201. While ^{201}T1 enjoys high myocardial extraction around 85%, extraction and retention of ^{201}T1 decrease as flow increases [2]. Teboroxime demonstrates even better myocardial extraction, with a first pass retention level of about 90%, and retains linear extraction even at flows up to 4.5 ml/min/g [3]. Teboroxime also undergoes fast washout from myocardial tissue [4–7], a property that may permit sequential stress / rest images to be acquired very quickly. However, such fast washout can be problematic for static imaging protocols, and the implications of this property are discussed further below. Teboroxime also demonstrates avid hepatic uptake which, though slower than its myocardial uptake, may adversely affect the apparent intensity of the inferior wall and increases the need for scatter compensation.

In addition to having very good physiological properties, ^{99m}*Tc*-teboroxime has imaging properties which are markedly better than those of ^{201}T1. ^{201}T1 has multiple emissions,

[1]This work was supported by NIH grant R01 HL50663.

primarily low energy (70–80 kev), which enhance degradation from attenuation and especially scatter. Furthermore, the relatively long physical half-life of ^{201}T1 (73.1h) greatly limits the acceptable dose due to radiation safety considerations, resulting in the need for longer acquisitions and exacerbating degradation from statistical noise. ^{99m} Tc, on the other hand, has an ideal emission energy (140 kev), good half-life (6.0h), and excellent imaging properties overall. Other ^{99m}Tc-labeled tracers, such as sestamibi [1], have received more attention than teboroxime, but the physiological properties of these tracers are limited compared to the full potential of teboroxime.

As alluded to earlier, the fast kinetics of teboroxime have several implications for cardiac imaging. Fast myocardial clearance permits multiple injections and sequential scans to be performed in short order, allowing stress / rest studies to be performed much more quickly than with other tracers [4,8]. However, teboroxime washout causes inconsistencies between projections acquired at different times during the scan, and differential washout between regions of normal and ischemic myocardium may cause streak artifacts and lead to an underestimation of ischemia when conventional static acquisitions are used [9]. Certain “multi-scan” static imaging protocols may potentially mitigate the former problem [10], for example acquiring ten 1 min. static scans and adding them together. On the other hand, the fast kinetics of teboroxime make it particularly well-suited for dynamic imaging protocols [11,12], where kinetic rate parameter estimates may potentially provide quantitative physiological information that is unavailable from static imaging.

The goal of this work was to comparatively evaluate multi-scan static teboroxime versus dynamic teboroxime myocardial perfusion SPECT in canines, with the underlying purpose of understanding the need for and potential benefit of the dynamic imaging approach. Eight dogs received dynamic ^{99m}Tc-teboroxime SPECT scans at rest and under adenosine stress. The left anterior descending (LAD) coronary artery was occluded in five of the animals. The data were analyzed using both compartmental-modeling dynamic processing and a multi-scan summed static processing method. For each study, washin rate parameters and static image intensities were correlated with microsphere-derived flow values in sixteen myocardial regions and compared.

II. METHODS

A. General Preparation

The canine studies used in this paper were performed as part of a larger protocol as described in [13], and only the details pertinent to this work are presented here. Studies were performed in eight canines (29.7 ± 8.1 kg), following the principles of laboratory animal care recommended by the NIH [14]. Each dog was initially anesthetized with 8 mg/kg Telazol (MWI Veterinary Supplies, Nampa, ID). The dogs were then intubated and anesthetized with oxygen mixed with halothane (1–10%). Heparin was administered at regular intervals, and small doses (3ml) of pancuronium, a muscle relaxant, were given as needed. The chest was opened at the 5th left intercostal space, and the heart was suspended in a pericardial cradle. A catheter, used for microsphere delivery, was placed in the left atrial appendage and secured with a purse-string suture. An ultrasonic flow probe was placed around the LAD between the first and second diagonal branches. In five animals the LAD was occluded with either a snare (n=4) or a hydraulic occluder (n=1) placed just distal to the flow probe. The snares and hydraulic occluder produced complete and partial occlusions, respectively. In order to minimize interference from liver uptake, gauze was placed above the liver to hold it away from the heart. This was done through a small slit in the abdomen. The chest was then closed, and the animal was moved to the imaging room for the duration of the study.

B. Data Acquisition

All imaging was performed on a PRISM 3000XP three detector system (Picker International) using 65 cm focal length LEHR fan beam collimators. The animal was first secured in a right lateral decubitus position on the imaging table. The blood pressure, ECG, and heart rate of each animal were monitored continuously throughout the study, and blood gases were measured periodically in order to avoid hypoxia.

Transmission imaging was performed first using a manufacturer-provided ^{153}Gd or ^{99m}Tc line source placed at the focal line of the collimator. The teboroxime scans were then acquired with a 15% energy window centered at 140 kev, and the data for each timeframe were binned into matrices of 64 bins × 64 slices × 120 angles using 0.712 cm pixels. The stress scan preceded the rest scan in four dogs, and it followed the rest scan in the other four dogs. The delay between the two scans was approximately 20 minutes, and the teboroxime dose was increased by (59 ±25)% for the second scan in order to reduce the effects of residual activity from the first scan. In both cases 180 serial acquisitions were acquired over 16.8 minutes by continuously rotating the three-head camera back-and-forth through 120°. The resultant data were combined to form 180 sets of 360° projection data, each acquired over 5.6 seconds. In all cases, at least one full timeframe was acquired prior to tracer injection.

For the resting studies, 13–31 mCi (490–1150 MBq) of ^{99m}Tc-teboroxime were administered intravenously. Approximately 1.3×10^6 microspheres, each 15 μm in diameter and labeled with ^{57}Co, were injected simultaneously into the left atrium. An arterial reference sample was withdrawn from the femoral artery at a rate of 7 ml/min, with the withdrawal beginning just prior to injection and lasting a minimum of 90 seconds.

For the stress studies, vasodilation with adenosine was used. In six animals the adenosine infusion was started prior to imaging, was adjusted during the initial 30 minutes to hold LAD flows stable at 3–4 times their resting values, and remained continuously on until SPECT imaging was complete. Initial adenosine infusion rates were approximately 50 μg/kg/min at a concentration of 5 mmol/L for these studies. In the other two dogs, adenosine stress was applied according to clinical patient protocol—adenosine was infused at a rate of 140 μg/kg/min for 6 minutes, with teboroxime injection occurring 3 minutes into the infusion period. Issues related to the differences between the continuous-infusion and clinical protocol infusion are discussed in detail in [15].

At the conclusion of each study, the animal was sacrificed and the heart excised. For animals with occlusions a staining procedure was used to mark the occluded region. Blue dye was injected into the LAD just distal to the occlusion, which was kept in place, and saline was injected simultaneously into the left main coronary artery at physiological pressure. The heart was then sectioned into six slices, each 7–10 mm thick, and photographed. Each slice was cut into quadrants or eighths, and the sections were weighed and placed into a vial for scintillation counting. The microsphere arterial reference samples were likewise placed in vials for subsequent counting. All samples were counted several days or later following the study in order to allow the radiopharmaceuticals to decay, and the microsphere data were decay-corrected back to the time of the imaging study.

C. Data Analysis

Reconstruction methods—The data for each study were processed in two ways: “multi-scan” summed static processing, and dynamic processing with compartmental modeling. Both methods used the reconstruction algorithm described here; the differences between the processing methods are described below. Recall that both stress and rest scans were performed in each animal during the same imaging period. In order to compensate for the residual activity

leftover from the first injection, the second scan acquired several timeframes before the second injection. The data from these timeframes were used for background-subtraction in the following manner. The background estimate was first reconstructed and then reprojected, a procedure which greatly reduces the effects of noise on each individual projection view. The reprojected data were then normalized and "subtracted" by adding them to the forward projection of the iterative reconstructions for the second scan. This procedure is essentially a background-subtraction method, but it maintains the Poisson statistical nature of the projection data [16,17].

All projection data were reconstructed using six iterations of the ordered-subsets expectation-maximization (OSEM) algorithm [18], with 10 angles per subset and stored on image matrices using cubic 5 mm voxels. The transmission data were reconstructed first and then scaled to the appropriate energies when necessary. The emission data were then reconstructed, using the transmission maps for non-uniform attenuation correction, and compensation for the depth-dependent detector-response function was also performed by modeling it in both the projector and backprojector of the algorithm. No scatter compensation was applied. The reconstructed images were reoriented and the region of the heart was extracted to form a series of approximately 15 short-axis slices. A semi-automated procedure [19] was used to generate septal, anterior, lateral, and inferior regions-of-interest (ROIs). Each ROI spanned pairs of adjacent short-axis slices, had an axial thickness of 1.0 cm, and had an average volume of 2.2 cm^3. In all, sixteen regions were used for each study.

Static image processing—For the static processing method, the timeframes for each study were summed angle-by-angle in various ways to produce ‘static-average’ datasets. The static-average data sums started at 0, 0.5, 1, 2, or 3 minutes post-injection, and were summed for durations of 0.5 to 10 minutes in either 30 second or one minute increments. Thus, 37 total static-average datasets were created for each study and reconstructed as described above. The best summing procedure was chosen as the one that maximized correlation with microsphere-derived flow values (as described below) over all studies.

One difficulty encountered when correlating static image intensities with blood flow is that image intensity is a quasi-quantitative measure that does not directly predict absolute flow values. An appropriate scale factor must be determined before correlation with blood flow can be calculated. Such scaling accounts for factors such as dose, body mass, imaging time, system sensitivity, extraction fraction, and physiological conditions. The scale factor differs for different imaging situations, and an accurate method of directly converting image intensity to blood flow is not currently available. One possibility is to use the integral blood curve as a normalization factor; however, we found that that method resulted in significantly lower overall correlation coefficients than the method described below. We make the assumption that, for each individual animal, the scale factors for the rest and stress studies differ only according to differences in the doses used. For each dog, the static ROI data from the stress study were first scaled by the ratio of rest/stress dose for that dog. The static ROI data from both the rest and stress scans were then scaled by a single scale factor so that the mean blood flow predicted by the static data was equal to the mean blood flow value measured using microspheres. Thus the inter-animal scale factors were chosen to maximize the overall correlation with flow.

Dynamic image processing—For the dynamic processing method, the projection data for each timeframe were reconstructed separately. Time-activity curves were calculated for each ROI using the time-series of reconstructed images. In addition, the blood input function were calculated using a ~4 cm^3 ROI placed in the left ventricle blood pool. These data were then fit to the two-compartment model shown in Figure 1 using RFIT [20,21]. Kinetic rate parameters for washin (k_{21}), washout (k_{12}), and vascular fraction in the ROI (f_v) were calculated by the fitting program. The governing equation for the two-compartment model is shown below:

$$A_i=(1-f_v)k_{21}\int_{t_i}^{t_i+\Delta t}\left[\int_0^{t_i+\Delta t} e^{-k_{12}\tau}B(t-\tau)d\tau\right]dt+f_v\int_{t_i}^{t_i+\Delta t}B(t)dt, \quad (1)$$

where A_i is the image intensity in the myocardial ROI for timeframe i, t_i is the time of the start of timeframe i, Δt is the duration of timeframe i, and $B(t)$ is the blood input function. The fitted washin parameters, k_{21}, in units of ml/min/ml were used for correlation with flow values for each study. One advantage of dynamic processing over static processing is that the dynamically estimated rate parameters are inherently quantitative, and the scaling issues encountered for the static processing method are avoided.

Microsphere-derived flows—Microsphere-derived myocardial blood flows were determined for each region using the methods of Heymann *et al.* [22]. The method included correction for cross-contamination between radiolabeled microspheres encountered during scintillation counting. Registration between the short-axis images and physical heart sections was accomplished visually using photographs of the excised heart sections. Only regions in the central four contiguous slices of the heart were considered, and the most apical and basal regions were discarded as registration errors were more likely in these slices. The microsphere-derived flows were used as the standard for imaging-versus-flow correlations.

III. RESULTS

Studies were successfully performed and analyzed in seven of the eight dogs. In one study the microsphere arterial reference sample was not successfully acquired, likely due to a blockage of the tubing used to acquire the sample. Since the required normalization of the microsphere data was not available, data for this dog were excluded from the analysis. Microsphere data from the remaining seven animals produced flow values within the expected ranges for both the rest and stress studies. Mean arterial pressure generally fell about 30% during adenosine infusion, and ST segment shift was noted with LAD occlusion.

A. Static Image Processing

Reconstructed image intensity was correlated with microsphere-derived flow values for each of the multi-scan summed static datasets. Recall that the summed static data started at either 0, 0.5, 1, 2, or 3 minutes post-injection and were summed for durations of 0.5 to 10 minutes in various increments. The correlation coefficients for each of these cases *vs.* flow are shown in Figure 2. In all cases, scan durations longer than 2 minutes produced monotonically decreasing correlation coefficients. The best summing procedure considered consisted of adding the projection data acquired from 60 to 180 seconds post-injection, and this dataset was used for all subsequent data analysis. Though the majority of the differences in mean correlation coefficient in Figure 2 were not statistically significant, the generally consistent trends suggest that the measured peak is likely near the true peak value.

It was somewhat unexpected that a scan of only 2 minutes length provided the best correlation with blood flow. Though initial teboroxime uptake is expected to correlate best with flow, we had anticipated that such a short scan duration would have insufficient statistics to provide the best performance. Figure 3 shows reconstructed short-axis slices for one of the stress studies for summed static data of 2 and 5 minutes duration. The noise levels in both of these sets of images are visually similar, though the mean number of counts in the 2 minute and 5 minute summed static data sets were 3.2×10^6 and 7.7×10^6, respectively. We postulate that the increase in statistics gained by including data acquired more than 3 minutes post-injection is offset by the poorer correlation with flow that such data exhibits; hence the shorter scan durations provide

better correlations with flow. Note that the situation may be somewhat different in humans, where larger body sizes and more attenuation may increase the need for higher statistics; however, the general trends observed here can be expected to hold for clinical studies as well.

B. Dynamic Imaging Results

The dynamic data for each study were successfully processed, except that the compartmental-model fitting program failed to converge for one region in one study. The data for that region were excluded from all subsequent analyses involving dynamic data. Sample time-activity curves for one of the stress studies showing the ROI uptake, input function, and fitted curve are given in Figure 4. The noise levels encountered were typical for dynamic SPECT imaging using fast rotation protocols, and fitted washin parameters fell within the expected range of physiologic blood flows at rest and under pharmacologic stress.

C. Correlation with Microsphere-Derived Flows

The correlation coefficients (r) for SPECT imaging results versus microsphere-derived flow values for each study are listed in Table 1. Here the rest and stress data for each dog were pooled, so each study contains 32 data points: 16 regions each at rest and at stress. In six out of seven dogs the dynamic imaging approach outperformed static imaging. The data were also pooled over all dogs and the results are shown on the bottom lines of Table 1 (223 data points for k_{21} *vs.* spheres, and 224 data points for static image intensity *vs.* spheres). These data are also plotted in Figure 5. For the pooled data, k_{21} was related to flow by $y = 0.632x + 0.383$, and scaled static image intensity was related to flow by $y = 0.574x + 0.630$. Note that the static results for the poled data are dependent upon the inter-study scaling procedure used. When the same inter-study scaling procedure was applied to the dynamic results (*i.e.*, scaling the rest +stress data for each dog so that the mean k_{21} values equals the mean microsphere-derived flow value), then the correlation of scaled-k_{21} *vs.* spheres was 0.872, and the fit was $y = 0.893x + 0.143$.

There are several possible reasons why the slopes of the regressions lines were considerably less than 1.0. For example, no scatter compensation was performed, and scattered photons would account for substantial bias in the reconstructed image values. Also, though the effect of partial volume interaction between myocardial tissue and blood is modeled in the compartmental modeling equation, partial volume interactions with the surrounding non-cardiac tissues would serve to bias the results. In previous work [23] we have found that scatter and partial-volume effects can significantly decrease washin parameter estimates. Thus such factors may be responsible for the decreased slopes of the regression lines observed in this work.

For each case listed in Table 1 the hypothesis H_0: $r_{k21} = r_{static}$ was tested versus the alternative H_A: $r_{k21} > r_{static}$ using the Fisher-*z* transformation and a one-tailed t-test [24]. The cases found to have statistically significant differences at the $\alpha=0.01$ level are marked in the table. Note that, for the data pooled across all studies, a significant difference between dynamic and static correlation with blood flow was observed ($p<.01$).

IV. DISCUSSION AND CONCLUSIONS

This study compared static versus dynamic teboroxime SPECT imaging of myocardial perfusion in canines using microsphere-derived flow values as the gold standard. In order to compare static and dynamic imaging under identical physiologic conditions, only dynamic scans were performed, which were then summed to create multi-scan static datasets. One consequence of this is that, though the summed static data accurately reflect the tracer distribution during the scanning period, they do not contain significant inconsistencies between

projection angles that would be encountered when using a conventional static scanning protocol. Such inconsistencies are a source of concern for teboroxime imaging because the tracer distribution changes significantly over the duration of the scan. The results of this work are therefore somewhat idealized for the static data, representing an upper limit on static imaging performance. In conventional practice a single static acquisition would be performed, which would be subject to errors not encountered here. It may be that the best way to perform static teboroxime imaging would be with a multi-scan summed approach such as used here, though much fewer and longer individual scans would likely be employed.

The dynamically determined washin rate parameter demonstrated a higher correlation with blood flow in six out of seven animals. When the data were pooled across all studies, dynamic imaging outperformed static imaging by a significant margin when inter-study scaling was applied to both datasets. When the dynamic data were treated as being truly quantitative, dynamic imaging still performed slightly better than static imaging even though the static data had ideal inter-study scaling applied and the dynamic data did not. Furthermore, the slopes of the regression fits were consistently closer to 1.0 for the dynamically processed data than for the static approach. These results lead us to conclude that dynamic SPECT imaging of teboroxime with compartmental-modeling may provide a more accurate measure of myocardial perfusion than does static imaging. The dynamic approach also carries the benefit that it provides measures of flow that are inherently quantitative, potentially providing objective measures for detecting disease that avoid subjective image interpretation.

Acknowledgments

The authors would like to thank Scott McJames and Steven G. Ross, Ph.D. for their help with the canine studies.

REFERENCES

1. Leppo JA, DePuey EG, Johnson LL. A review of cardiac imaging with sestamibi and teboroxime. J. Nucl. Med 1991;vol. 32:2012–2022. [PubMed: 1833519]
2. Leppo JA, Meerdink DJ. Comparative myocardial extraction of two technetium-labeled BATO derivatives (SQ30217, SQ32014) and thallium. J. Nucl. Med 1990;vol. 31:67–74. [PubMed: 2295943]
3. Narra RK, Nunn AD, Kuczynski BL, Feld T, Wedeking P, Eckelman WC. A neutral technetium-99m complex for myocardial imaging. J. Nucl. Med 1989;vol. 30:1830–1837. [PubMed: 2809747]
4. Stewart RE, Schwaiger M, Hutchins GD, Chiao P-C, Gallagher KP, Nguyen N, Petry NA, Rogers WL. Myocardial clearance kinetics of technetium-99m-SQ30217: a marker of regional myocardial blood flow. J. Nucl. Med 1990;vol. 31:1183–1190. [PubMed: 2362197]
5. Beanlands R, Muzik O, Nguyen N, Petry N, Schwaiger M. The relationship between myocardial retention of technetium-99m teboroxime and myocardial blood flow. J. Am. Coll. Cardiol 1992;vol. 20:712–719. [PubMed: 1512353]
6. Weinstein H, Dahlberg ST, McSherry BA, Hendel RC, Leppo JA. Rapid redistribution of teboroxime. Am. J. Cardiol 1993;vol. 71:848–852. [PubMed: 8456765]
7. Chua T, Kiat H, Germano G, Palmas W, Takemoto K, Friedman J, Berman DS. Technetium-99m teboroxime regional myocardial washout in subjects with and without coronary artery disease. Am. J. Cardiol 1993;vol. 72:728–734. [PubMed: 8249853]
8. Chua T, Kiat H, Germano G, Takemoto K, Fernandez G, Biasio Y, Friedman J, Berman D. Rapid back to back adenosine stress-rest Tc-99m teboroxime myocardial perfusion SPECT using a triple-detector camera. J. Nucl. Med 1993;vol. 34:1485–1493. [PubMed: 8355068]
9. Links JM, Frank TL, Becker LC. Effect of differential tracer washout during SPECT acquisition. J. Nucl. Med 1991;vol. 32:2253–2257. [PubMed: 1824556]
10. Nakajima K, Taki J, Bunko H, Matsudaira M, Muramori A, Matsunari I, Hisada K, Ichihara T. Dynamic acquisition with a three-headed SPECT system: application to technetium 99m SQ30217 myocardial imaging. J. Nucl. Med 1991;vol. 32:1273–1277. [PubMed: 2045946]

11. Gullberg, GT.; Huesman, RH.; Ross, SG.; DiBella, EVR.; Zeng, GL.; Reutter, BW.; Christian, PE.; Foresti, SA. Dynamic cardiac single photon emission computed tomography. In: Zaret, BL.; Beller, GA., editors. Nuclear Cardiology: State of the Art and Future Directions. New York: Mosby-Year Book; 1998. p. 137-187.
12. Smith AM, Gullberg GT, Christian PE, Datz FL. Kinetic modeling of teboroxime using dynamic SPECT imaging of a canine model. J. Nucl. Med 1994;vol. 35:484–495. [PubMed: 8113904]
13. DiBella EVR, Ross SG, Kadrmas DJ, Khare HS, Christian PE, McJames S, Gullberg GT. Compartmental modeling of technetium-99m-labeled teboroxime with dynamic SPECT: comparison to static T1-201 in a canine model. preparation. 1999
14. National Institutes of Health. NIH Guide for the care and use of laboratory animals. 1996
15. DiBella EVR, Khare HS, Kadrmas DJ, Gullberg GT. SPECT imaging of teboroxime during myocardial blood flow changes. IEEE Trans. Nucl. Sci. 2000 accepted for publication.
16. Bowsher JE, Johnson VA, Turkington TG, Jaszczak RJ, Floyd CE Jr, Coleman RE. Bayesian reconstruction and use of anatomical a priori information for emission tomography. IEEE Trans. Med. Imag 1996;vol. 15:673–686.
17. Lange K, Carson R. E.M. reconstruction algorithms for emission and transmission tomography. J. Comput. Assist. Tomog 1984;vol. 8:306–316.
18. Hudson HM, Larkin RS. Accelerated image reconstruction using ordered subsets of projection data. IEEE Trans. Med. Imag 1994;vol. 13:601–609.
19. DiBella EVR, Gullberg GT, Barclay AB, Eisner RL. Automated region selection for analysis of dynamic cardiac SPECT data. IEEE Trans. Nucl. Sci 1997;vol. 44:1355–1361.
20. Huesman RH, Mazoyer BM. Kinetic data analysis with a noisy input function. Phys. Med. Biol 1987;vol. 32:1569–1579. [PubMed: 3501592]
21. Huesman, RH.; Knittel, BL.; Mazoyer, BM.; Coxson, PG.; Salmeron, EM.; Klein, GJ.; Reutter, BW.; Budinger, TF. Notes on RFIT: a program for fitting compartment models to region-of-interest dynamic emission tomography data. Berkeley, CA: Lawrence Berkeley National Laboratory; 1995.
22. Heymann MA, Payne BD, Hoffman JE, Rudolph AM. Blood flow measurements with radionuclide-labeled particles. Prog. Cardiovasc. Dis 1977;vol. 20:55–79. [PubMed: 877305]
23. Kadrmas DJ, DiBella EVR, Huesman RH, Gullberg GT. Analytical propagation of errors in dynamic SPECT: estimators, degrading factors, bias and noise. Phys. Med. Biol 1999;vol. 44:1997–2014. [PubMed: 10473210]
24. Zar, JH. Biostatistical Analysis. Upper Saddle River, NJ: Prentice-Hall, Inc.; 1999.

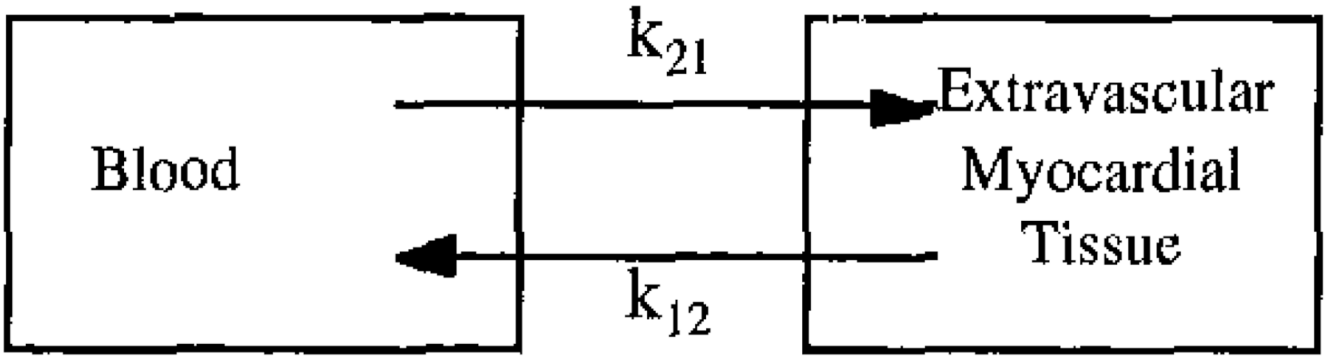

Figure 1.
A two-compartment model for the exchange of teboroxime between the blood and extravascular myocardial tissue.

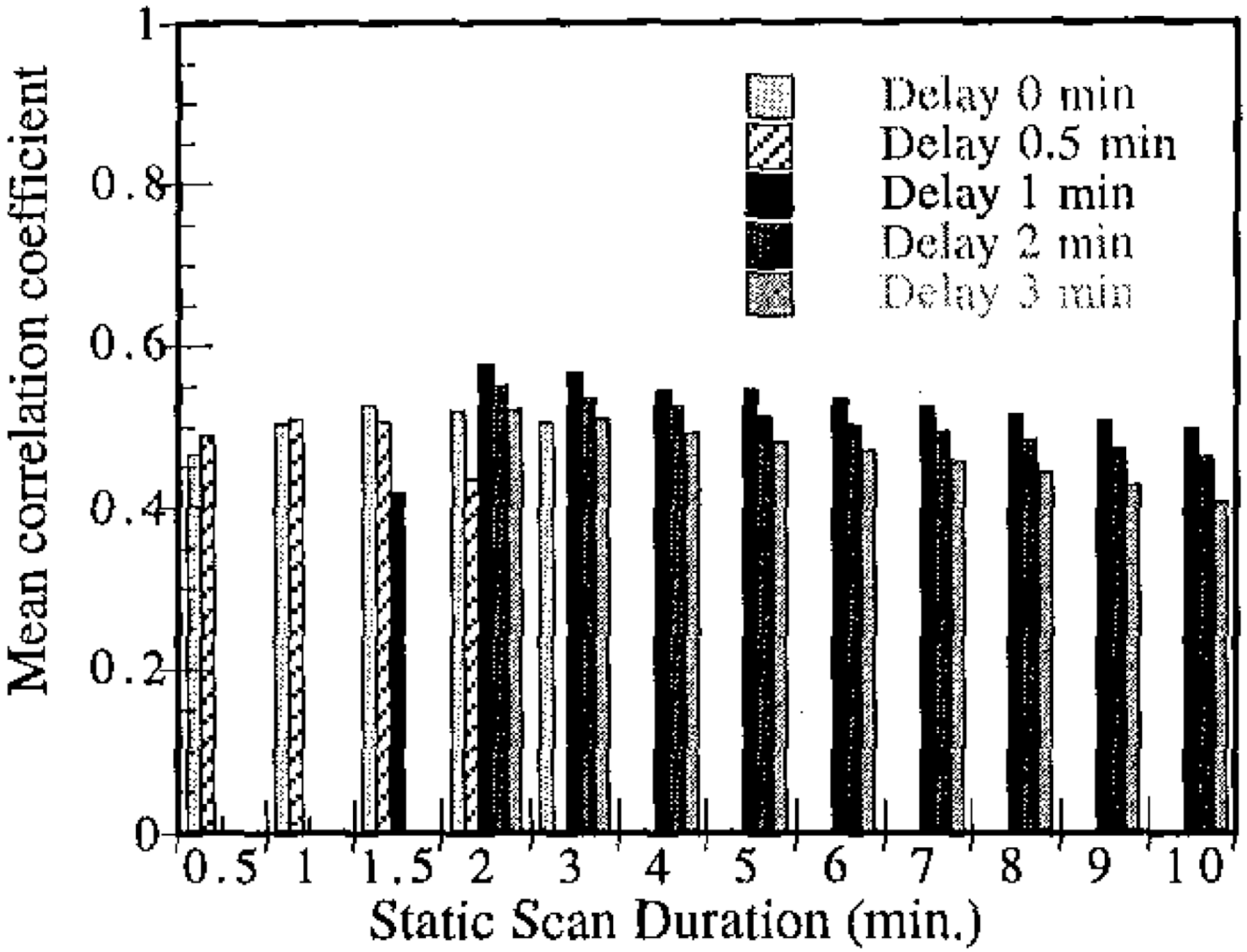

Figure 2.
Mean correlation coefficient for static image intensity *vs.* blood flow in all studies shown as a function of summed static scan duration and delay post-injection.

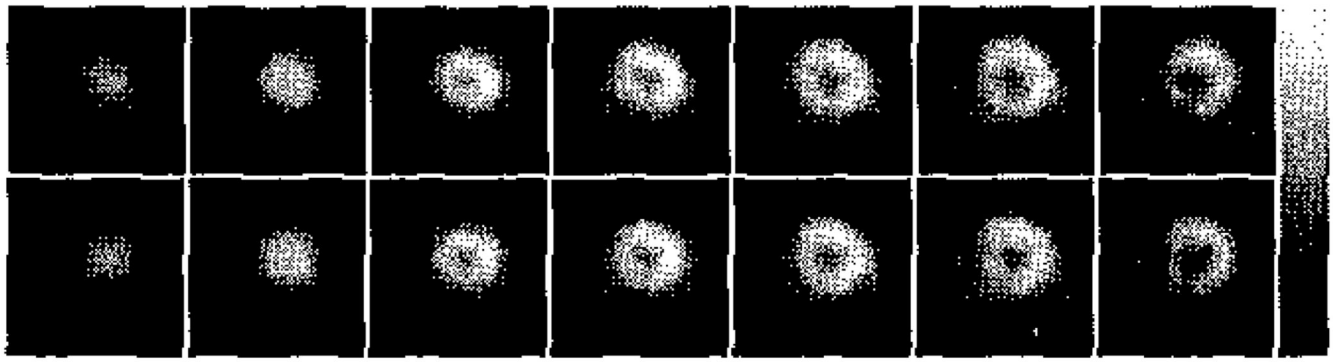

Figure 3.
Reconstructed short-axis slices for one of the stress studies for summed static data of 2 minutes (top row) and 5 minutes (bottom row) duration. A delay of 1 minute post-injection was used. Note that the noise levels in both sets of images appear similar.

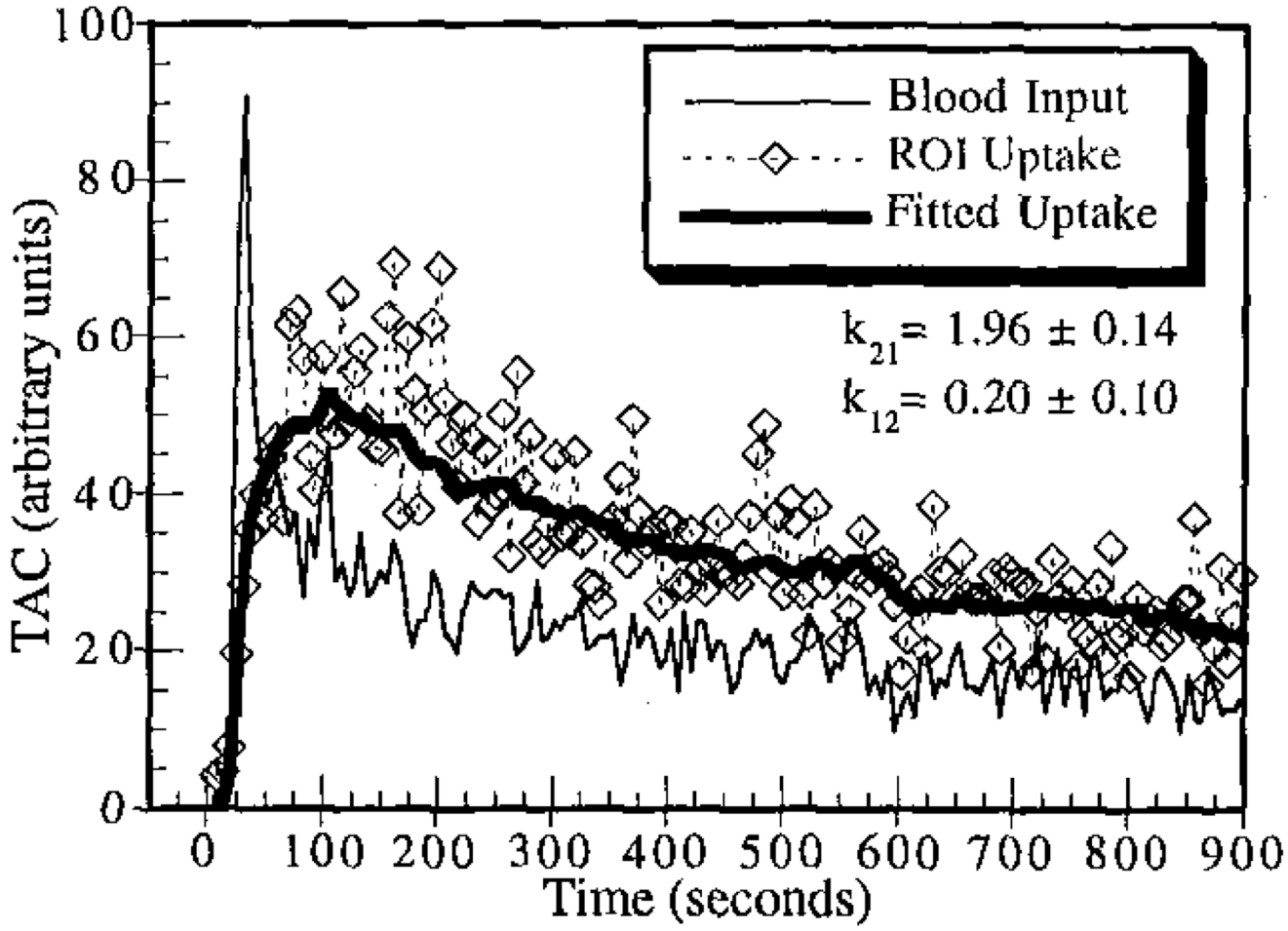

Figure 4.
Sample time-activity curves for one of the stress studies. The fitted washin and washout parameters are shown.

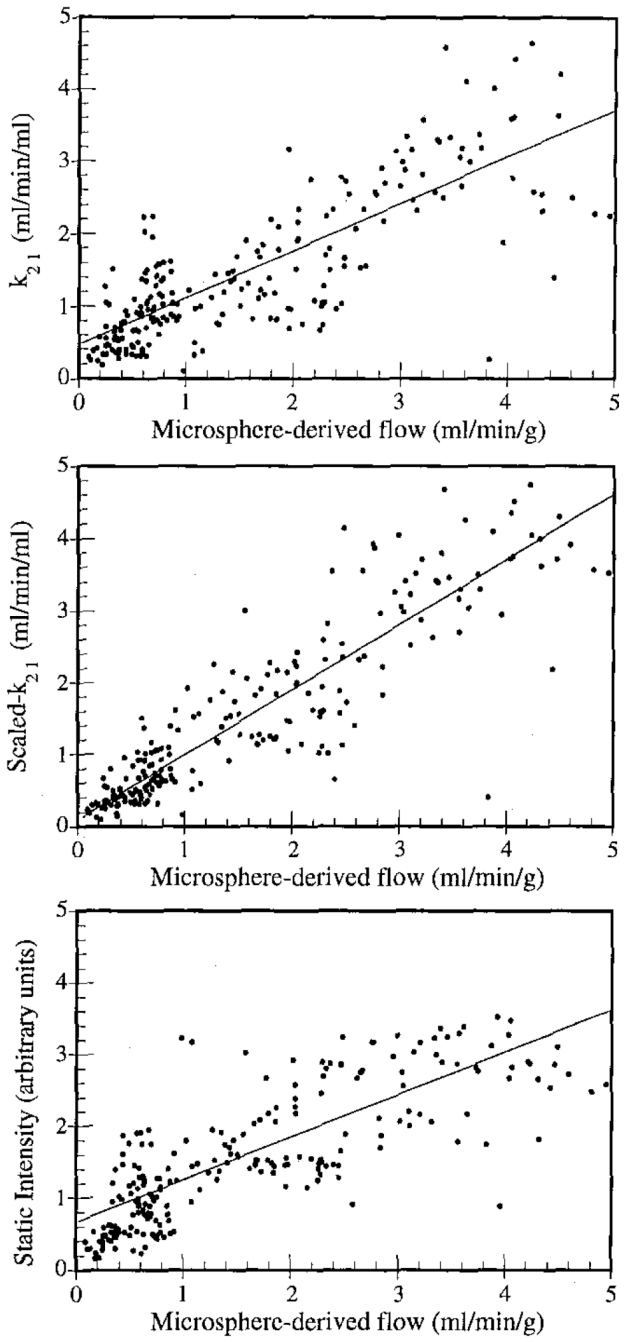

Figure 5.
Correlation plots of SPECT imaging results *vs.* microsphere-derived flows showing data pooled for all studies: unscaled washin parameter k_{21} (top), inter-study scaled washin parameter k_{21} (middle), and scaled static image intensity (bottom). The fitted regression lines are also shown for each case.

Table 1

SPECT imaging correlations with microspheres for each canine.

Study No.	k_{21} *vs.* Spheres	Static *vs.* Spheres
1	0.945	0.913
2	0.964*	0.852*
3	0.607	0.393
4	0.565	0.607
5	0.738	0.685
6	0.810*	0.443*
7	0.706	0.477
All Studies	0.795	N/A
All Studies, with inter-study scaling	0.872*	0.792*

* significantly different at α=0.01 level